Bulletin of the Seismological Society of America, Vol. 99, No. 2B, pp. 1378–1390, May 2009, doi: 10.1785/0120080070

Empirical Scaling of Rotational Spectra of Strong Earthquake Ground Motion

by V. W. Lee and M. D. Trifunac

Abstract Many empirical scaling equations have been developed for scaling Fourier spectrum amplitudes of strong earthquake accelerations and for generation of artificial strong-motion accelerograms for the translational, torsional, and rocking components of strong motion. It has also been shown that rotational components of strong motion significantly contribute to the overall response of structures; however, little progress has been made in the development and deployment of strong-motion instruments to measure rotations. This article presents a simple approximate algorithm for generating torsional and rocking Fourier spectral amplitudes from the corresponding translational motions. The method can be used to generate torsion and rocking spectra from the translational Fourier spectra of actual records. Inverse Fourier transform can be used to generate torsional and rocking time histories.

Introduction

After 75 years of strong-motion recording programs in the western United States and up to 40 years in many other parts of the world, several thousand strong-motion accelerograms have been recorded, processed, and made available for distribution (Trifunac, 2007). The observational strong-motion programs evolved in the early 1900s from the realization that it is essential to record strong ground motions during actual earthquakes (Hudson, 1983a,b; Trifunac, 2009a) to guide the development of the methods for analysis and prediction of structural response and to provide a basis for experimental verification of the theoretical models. The strong-motion database accumulated so far allows earthquake engineers to (1) study the strong motion in different parts of the world to gain understanding of its characteristics and destructive potential in relation to the tectonic characteristics of the areas where earthquakes occur, (2) analyze and interpret the dynamic response of structures during earthquakes, (3) identify and quantify the earthquake strong-motion parameters associated with generation and transmission of strong-motion waves, and (4) provide a data bank for future studies.

While the recorded data are invaluable for research and analyses of strong motion, they still do not cover many different recording conditions, which are needed for engineering design. This is particularly true in those areas that have low seismic activity and have thus not yet accumulated an adequate strong-motion database. It is also often necessary to estimate future shaking at sites, which may have characteristics outside the range of parameters for which the recorded data are now available. It was for these reasons that serious development of modern empirical scaling equations for direct scaling of Fourier and response-spectral amplitudes began following the successful recording of the San Fernando, California, earthquake of 1971 (Trifunac, 1976; Lee, 2002a,b, 2007). The work on direct empirical scaling of spectral amplitudes also facilitated the development of the algorithms for generation of synthetic strong-motion accelerograms of translational components of strong motion (Trifunac, 1971; Wong and Trifunac, 1979). In addition, it was recognized that the torsional and rocking components of strong motion, acting together with the translations, significantly contribute to the overall response of structures during strong shaking (Kobori and Shinozaki, 1973; Luco, 1976; Lee, 1979). In the absence of programs to develop instruments to record the rotational components of strong motion, it became necessary to estimate the rotational motions in terms of the corresponding translational motions. Trifunac (1982) showed how the torsion and rocking of the ground surface associated with incident body waves can be determined in terms of the corresponding translational amplitudes of motion. Then, a few years later, Lee and Trifunac (1985, 1987) showed how to generate synthetic torsional and rocking accelrograms, along with their Fourier and response spectra, starting from the amplitudes of horizontal motions.

During the past two decades, in spite of the fact that engineering studies have continued to show the significance of the rotational components in strong-motion excitation for the response of structures (Kalkan and Graizer, 2007a,b; Trifunac, 2006, 2008), the progress in developing and deploying strong-motion instruments that can also record rotational components of earthquake waves has continued to be slow. In this article, we first briefly review our approach for the generation of artificial translational and rotational accelerograms; then we present an approximate method for its exten-

sion to generation of rotational Fourier spectra of strong earthquake motion. We also present examples of the empirical scaling equations of torsional and rocking spectra, along with the corresponding rotational time histories.

Synthetic Translational, Torsional, and Rocking Accelerograms

A review of our method for the generation of synthetic accelerograms can be found in Lee (2002b). It is based on the superposition of dispersed elastic waves, and it generates the rotational components of motion, the strains, and the curvatures in terms of their analytic relationship to the amplitudes of the translational motions. The synthetic translational components of acceleration are constructed to have the required Fourier amplitude spectrum, FS(ω), and a given duration (Trifunac, 1971; Wong and Trifunac, 1979).

Dispersion Curves

For a given site, a model of its geological characteristics in terms of an equivalent layered medium is first selected. A model can have L layers, and for each layer i, with $i = 1$ to L, the parameters h_i, α_i, β_i, and ρ_i, the thickness, the P-wave velocity, the S-wave velocity, and the density, with the bottom ($i = L$) medium of infinite thickness, must be specified. In a layered medium, surface waves travel in a dispersive manner, while the phase velocities of body waves can be determined from path geometry. The dispersion curves of the Rayleigh and Love surface waves are then evaluated; the results consist of $m = 1, 2, 3\ldots, M$ phase and group velocities, $C_m(\omega_n)$ and $U_m(\omega_n)$, determined at a discrete set of frequencies, ω_n, $n = 1, 2, \ldots, N$.

Arrival Times

The arrival time of the energy in the mth mode at frequency ω_n can be written as $t^*_{nm} = R/U_m(\omega_n)$, where R is epicentral or some representative distance from the source to the site. For computational efficiency, this arrival time t^*_{nm} is assumed to hold for a frequency band $\omega_n \pm \Delta\omega_n$, narrow enough for $U_m(\omega_n)$ to be approximated by a constant. Furthermore, for simplicity in formulation of the algorithms, we treat the body P and S waves as $M + 1$st modes of surface waves, but with frequency-independent (i.e., constant) velocities.

Contribution of the Modes at a Given Frequency Band

Within the frequency band $\omega_n \pm \Delta\omega_n$, the mth mode of surface waves with relative amplitude A_{nm} has a Fourier transform (Trifunac, 1971; Wong and Trifunac, 1979)

$$A_{nm}(\omega) = \begin{cases} \frac{\pi}{2} A_{nm} \exp[-i(\omega - \omega_n)t^*_{nm} + i\phi_n] \\ \qquad \text{for } |\omega - \omega_n| \le \Delta\omega_n, \\ 0, \qquad \text{otherwise.} \end{cases} \tag{1}$$

All Fourier transforms considered in this article are from real-valued functions that satisfy the implicit identity $A_{nm}(-\omega) = A^*_{nm}(\omega)$; thus, they need to be defined only for $\omega > 0$. The phase ϕ_n is taken as random, between $-\pi$ and $+\pi$, and is introduced to model the source and randomness encountered along the wave path. At the site, t^*_{nm} is the arrival time of the mth mode at frequency ω_n. A_{nm} is the relative amplitude of the mth mode at the same frequency.

The inverse transform of equation (1) is

$$\begin{aligned} a_{nm}(t) &= \frac{1}{2\pi}\int_{-\infty}^{\infty} A_{nm}(\omega) e^{i\omega t} d\omega \\ &= A_{nm}\frac{\sin \Delta\omega_n(t - t^*_{nm})}{(t - t^*_{nm})}\cos(\omega_n t + \phi_n), \end{aligned} \tag{2}$$

which represents the contribution to the time signal of the mth mode at frequency ω_n. The total contribution of all the modes is

$$\begin{aligned} a_n(t) &= \sum_{m=1}^{M} \alpha_n a_{nm}(t) \\ &= \sum_{m=1}^{M} \alpha_n A_{nm}\frac{\sin \Delta\omega_n(t - t^*_{nm})}{(t - t^*_{nm})}\cos(\omega_n t + \phi_n), \end{aligned} \tag{3}$$

where M is the total number of surface wave modes to be considered, and α_n is the scaling factor that will be used to determine the final amplitude of FS(ω_n).

Determination of A_{nm} and α_n

The relative amplitudes of different modes of contributing surface waves, A_{nm}, depend upon the source mechanism and the propagation path; they cannot be deterministically estimated due to the unknown fine structure of the medium through which the waves propagate. Thus, we qualitatively estimate these amplitudes on the basis of past recordings. The following empirical estimates forA_{nm} were proposed by Trifunac (1971) and will be used in the examples of this article as well.

$$\begin{aligned} &A_{nm} = A_{nm}(\omega_n) = A_1(m)A_2(\omega_n), \\ &\text{where } \begin{cases} A_1(m) &= |\exp[-(m - m_0)^2/2C_0^2] + C_R X_m| \\ A_2(\omega_n) &= |B_0 \exp[-(\omega - \omega_p)^2/2\omega_B^2] + B_R X_n| \end{cases}, \end{aligned} \tag{4}$$

with X_m and X_n random numbers in $[-1, 1]$. Example values of the scaling coefficients are given in Table 1.

The scaling factor α_n is determined so that the spectra of synthesized accelerograms agree with some given or empirically determined Fourier amplitudes. The Fourier amplitude of the transform of $a_n(t)$ in equation (3) is

Table 1
Empirical Scaling Coefficients for Equation (4)

Mode	C_0	m_0	C_R	B_0	ω_P	ω_B	B_R
1	3	5	0.2	1.5	10	5	0.1
2	3	5	0.2	1.5	10	5	0.1
3	3	5	0.2	1.5	10	5	0.1
4	3	5	0.2	2.0	25	15	0.1
5	3	5	0.2	2.0	25	15	0.1
6	3	6	0.2	3.0	30	10	0.3
7	3	7	0.2	1.5	30	5	0.25

From Trifunac (1971).

$$A_n(\omega) = \begin{cases} \sum_{m=1}^{M} \frac{\pi}{2} \alpha_n A_{nm} \exp[-i(\omega - \omega_n)t^*_{nm} + i\phi_n] \\ \qquad \text{for } |\omega - \omega_n| \le \Delta\omega_n, \\ 0, \qquad \text{otherwise} \end{cases} \tag{5}$$

for $0 \le \omega < \infty$, and $|A_n(-\omega)| = |A_n(\omega)|$. $|A_n(\omega)|$ is defined only over the frequency band $\omega_n \pm \Delta\omega_n$ of width $2\Delta\omega_n$. Its mean amplitude over this range, $\overline{|A_n(\omega)|} = \frac{1}{2\Delta\omega} \int_{\omega_n - \Delta\omega_n}^{\omega_n + \Delta\omega_n} |A_n(\omega)| d\omega$, is then set to agree with the given or empirically determined Fourier amplitude, $\widehat{\mathrm{FS}}(\omega_n)$. Setting $\overline{|A_n(\omega)|} = \widehat{\mathrm{FS}}(\omega_n)$ gives

$$\alpha_n = 2\Delta\omega_n \widehat{\mathrm{FS}}(\omega_n) / \frac{\pi}{2} \times \int_{\omega_n - \Delta\omega_n}^{\omega_n + \Delta\omega_n} \left| \sum_{m=1}^{M} A_{nm} \exp[-i(\omega - \omega_n)t^*_{nm} + i\phi_n] \right| d\omega. \tag{6}$$

The Fourier amplitude $\widehat{\mathrm{FS}}(\omega_n)$ at frequency ω_n may be estimated from the empirical scaling equations and by using the parameters that describe the site (Trifunac, 1976, 1989a,b, 1990, 1991; Lee and Trifunac, 1995).

Total Translational Accelerogram

The total Fourier transform and the total acceleration-time history are then expressed as

$$A(\omega) = \sum_{n=1}^{N} A_n(\omega) \qquad \text{and}$$

$$a(t) = \sum_{n=1}^{N} a_n(t) = \sum_{n=1}^{N} \sum_{m=1}^{M} \alpha_n a_{nm}(t) = \sum_{n=1}^{N} \alpha_n \left(\sum_{m=1}^{M} A_{nm} \frac{\sin \Delta\omega_n (t - t^*_{nm})}{(t - t^*_{nm})} \right) \cos(\omega_n t + \phi_n), \tag{7}$$

with N the total number of frequency bands.

Generation of Synthetic Torsional Accelerograms

Lee and Trifunac (1985) extended the aforementioned approach to empirical estimation of torsional accelerograms. The results in Trifunac (1982) were used to calculate torsion from body *SH* and surface Love waves. The torsional motion $\psi(x, y, t)$ at ground surface ($y = 0$) is related to the transverse displacement $w(x, y, t)$ of *SH* and Love waves by (Trifunac, 1982)

$$\psi|_{y=0} = \frac{-i\omega}{2c_x} w \Big|_{y=0}, \tag{8}$$

where ω and c_x are the frequency and horizontal phase velocity of the waves. With given Fourier amplitude of the translational motions, the Fourier spectrum of the corresponding torsional motion can be determined by using equation (8). Starting with the Fourier transform of the mth mode of surface waves in the frequency band $\omega_n \pm \Delta\omega_n$, which is given by equation (2), the corresponding torsional motion becomes

$$\Psi_{nm}(\omega) = \begin{cases} \frac{-i\omega\pi}{4c_{nm}} A_{nm} \exp[-i(\omega - \omega_n)t^*_{nm} + i\phi_n] \\ \qquad \text{for } |\omega - \omega_n| \le \Delta\omega_n, \\ 0 \qquad \text{otherwise,} \end{cases} \tag{9}$$

with $\Psi_{nm}(-\omega) = \Psi^*_{nm}(\omega)$, where $c_{nm} = c_m(\omega_n)$ is the phase velocity of the mth mode of Love waves, assumed to be constant within the frequency band $\omega_n \pm \Delta\omega_n$. Combining all of the modes of Love waves and body *SH* waves, the rotational motion in this frequency band is

$$\Psi_n(\omega) = \begin{cases} \frac{-i\omega\pi}{4} \alpha_n \sum_{m=1}^{M} \frac{A_{nm}}{c_{nm}} \exp[-i(\omega - \omega_n)t^*_{nm} + i\phi_n] \\ \qquad \text{for } |\omega - \omega_n| \le \Delta\omega_n, \\ 0 \qquad \text{otherwise,} \end{cases} \tag{10}$$

where α_n is the scaling factor given in equation (6). The total Fourier transform of the torsional accelerogram is then $\Psi(\omega) = \sum_{n=1}^{N} \Psi_n(\omega)$. The corresponding torsional time histories $\psi(t)$ can then be computed by inverse Fourier transform.

Generation of Rocking Accelerograms

Lee and Trifunac (1987) next extended this approach to the generation of rocking accelerations in terms of rocking motion $\phi(x, y, t)$ at the ground surface ($y = 0$) and vertical displacement $v(x, y, t)$ corresponding to body *P* and *SV* waves and to surface Rayleigh waves:

$$\phi|_{y=0} = \frac{i\omega}{c_x} v \Big|_{y=0}. \tag{11}$$

Starting with the Fourier transform of the vertical translation, as given by equation (2), the mth mode of rocking within the frequency band $\omega_n \pm \Delta\omega_n$ is

$$\Phi_{nm}(\omega) = \begin{cases} \frac{i\omega\pi}{2c_{nm}} A_{nm} \exp[-i(\omega-\omega_n)t^*_{nm} + i\phi_n] \\ \qquad \text{for } |\omega-\omega_n| \le \Delta\omega_n, \\ 0 \qquad \text{otherwise,} \end{cases} \tag{12}$$

with $\Phi_{nm}(-\omega) = \Phi^*_{nm}(\omega)$, where $c_{nm} = c_m(\omega_n)$ is the phase velocity of the body waves or of the mth mode of surface Rayleigh waves. It is assumed that it is constant within the frequency band $\omega_n \pm \Delta\omega_n$. Combining all of the contributing modes of Rayleigh and body S and P waves, the rocking motion in this frequency band then becomes

$$\Phi_n(\omega) = \begin{cases} \frac{i\omega\pi}{2} \alpha_n \sum_{m=1}^{M} \frac{A_{nm}}{c_{nm}} \exp[-i(\omega-\omega_n)t^*_{nm} + i\phi_n] \\ \qquad \text{for } |\omega-\omega_n| \le \Delta\omega_n, \\ 0, \qquad \text{otherwise,} \end{cases} \tag{13}$$

where α_n is the scaling factor given in equation (6), now with respect to the vertical component of motion. The total Fourier transform of the rocking accelerogram is $\Phi(\omega) = \sum_{n=1}^{N} \Phi_n(\omega)$, with the corresponding rocking time histories $\phi(t)$ by inverse Fourier transform.

The Ratios of Rotational to Translational Fourier Spectra

Having summarized the relationships among the empirical scaling equations of the rotational and translational Fourier spectra allows us to generate the time histories of the rotational components from the corresponding translational components of strong motion. Once the rotational time histories are generated, the corresponding rotational response spectra can also be calculated.

Ratio of Torsional to Horizontal Transverse Fourier Spectra

Equation (9) shows that the ratio of the torsional motion, $\Psi(\omega)$, to the corresponding transverse horizontal motion, $H(\omega)$, is

$$\frac{\Psi(\omega)}{H(\omega)} = \frac{-i\omega}{2c(\omega)}, \quad \text{with amplitude} \quad \left|\frac{\Psi(\omega)}{H(\omega)}\right| = \frac{\omega}{2c(\omega)}, \tag{14}$$

where $c(\omega)$ is the horizontal phase velocity.

As an illustration, we consider a seven-layer model (Table 2) that corresponds to a site in El Centro, California. Dispersion curves for this site were computed using the Haskell–Thomson matrix method (Thomson, 1950; Haskell, 1953), which generated the phase and group velocity curves for Rayleigh and Love waves. The five solid curves in Figure 1 from the right are for the first five modes of the Rayleigh waves. Mode 1 is the right-most solid curve, followed by modes 2–5 to the left. The same holds for the five modes of Love waves, which are plotted with dashed lines. At short periods, all curves approach the minimum S-wave velocity (in this example, 0.30 km/sec). The two left-most curves

Table 2
Layered Medium near El Centro, California

Layer Number	Depth (km)	α	β	Density (g/cc)
1	0.05	0.60	0.30	1.20
2	0.13	1.70	0.98	1.28
3	0.55	1.96	1.13	1.36
4	0.98	2.71	1.57	1.59
5	1.19	3.76	2.17	1.91
6	2.68	4.69	2.71	2.19
7	∞	6.40	3.70	2.71

From Lee and Trifunac (1985) and (1987).
α, β: P- and S-wave velocities (km/sec).

model body waves, with the dashed S wave below the solid P wave on top. The body S wave is chosen to start at the minimum c_β, in this example, 0.30 km/sec at period near 0.1 sec, and to quickly rise to the maximum c_β at 3.7 km/sec. The body P wave similarly starts at the minimum c_α, 0.6 km/sec, and quickly rises to the maximum c_α at 6.4 km/sec. Both are included in this figure and in the calculations as the sixth and seventh modes of surface waves.

Next we consider the transverse components of Love waves and the corresponding torsional waves. From equations (5) and (10), the waves corresponding to their mth mode, for frequencies within $|\omega-\omega_n| \le \Delta\omega_n$, are

$$H_{nm}(\omega) = A_{nm}(\omega) = \frac{\pi}{2} A_{nm} \exp[-i(\omega-\omega_n)t^*_{nm}] \exp(i\phi_n),$$
$$\Psi_{nm}(\omega) = \frac{\pi}{2}\left(\frac{-i\omega}{2c_{nm}}\right) A_{nm} \exp[-i(\omega-\omega_n)t^*_{nm}] \exp(i\phi_n), \tag{15}$$

where $c_{nm} = c_m(\omega_n)$ is the Love-wave phase velocity of the mth mode at frequency $\omega = \omega_n$. From equation (15), their ratio takes the following form, as in equation (14):

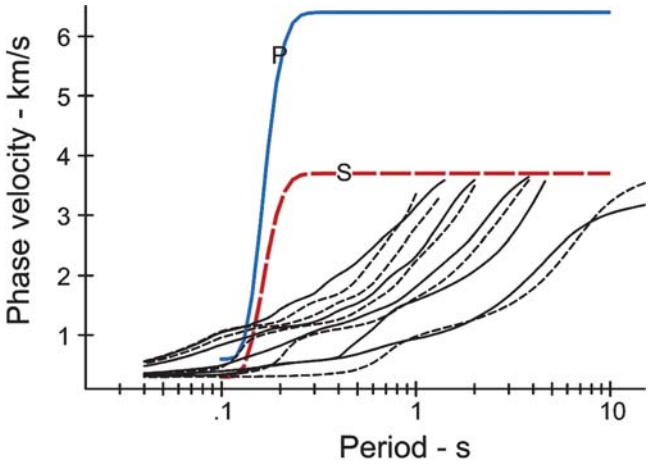

Figure 1. Love (dashed lines) and Rayleigh (solid lines) surface wave phase velocity curves for the El Centro site in California. Model P- and S-wave velocities are also shown.

$$\frac{\Psi_{nm}(\omega)}{H_{nm}(\omega)} = \frac{-i\omega}{2c_{nm}}, \quad \text{with amplitude} \quad \left|\frac{\Psi_{nm}(\omega)}{H_{nm}(\omega)}\right| = \frac{\omega}{2c_{nm}}. \tag{16}$$

Figure 2 shows a plot of these ratios, $\omega/2c_m(\omega)$, for the five modes of Love waves plus body S waves as the sixth mode. The curves for the six modes all have similar slopes, especially at high frequency, along the straight dashed line joining the limits of $\omega/2\beta_{\max}$ at the low-frequency end and $\omega/2\beta_{\min}$ at the high-frequency end. This is an important linear trend that we exploit further in this article.

A simple way to characterize the ratio, $\Psi(\omega)/H(\omega)$, with all of the modes of Love waves and body S waves combined, can be derived from their definition. In each of the n frequency bands, $\omega_n \pm \Delta\omega_n$, considering M modes, within $|\omega - \omega_n| \le \Delta\omega_n$, we have

$$\begin{aligned} H_n(\omega) &= A_n(\omega) \\ &= \frac{\pi}{2}\alpha_n \left\{ \sum_{m=1}^{M} A_{nm} \exp[-i(\omega-\omega_n)t^*_{nm}] \right\} \exp(i\phi_n), \\ \Psi_n(\omega) &= \frac{\pi}{2}\alpha_n \left\{ \sum_{m=1}^{M} \left(\frac{-i\omega}{2c_{nm}}\right) A_{nm} \exp[-i(\omega-\omega_n)t^*_{nm}] \right\} \\ &\quad \times \exp(i\phi_n). \end{aligned} \tag{17}$$

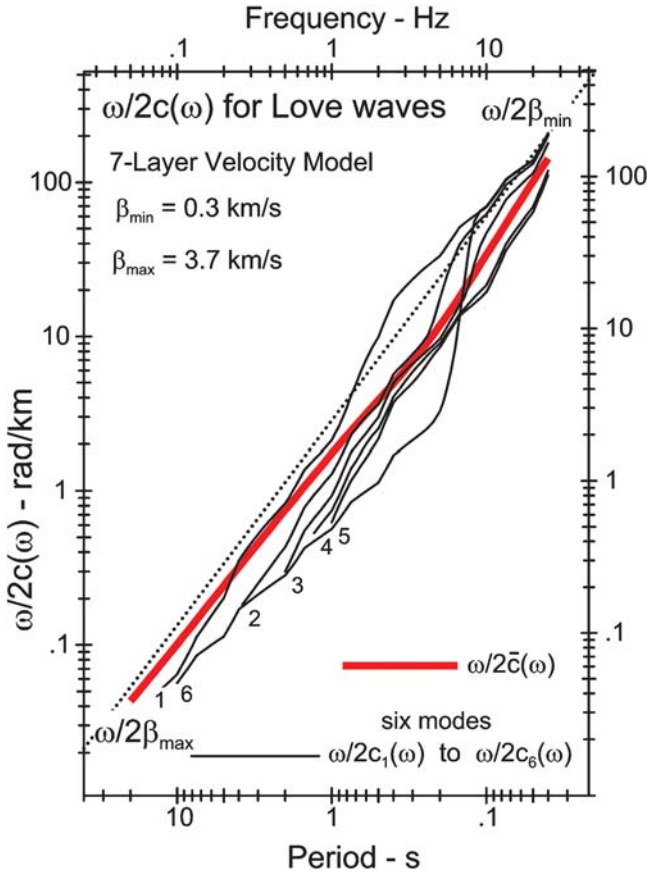

Figure 2. Ratio of frequency to phase velocities for the five modes (1–5) of Love waves, and for S waves as sixth mode (6), for a 7-layer velocity model.

Equation (17) can be used to compute the ratio $\Psi(\omega)/H(\omega)$ within $\omega_n \pm \Delta\omega_n$:

$$\begin{aligned} \left.\frac{\Psi(\omega)}{H(\omega)}\right|_{\omega=\omega_n} &= \frac{\Psi(\omega_n)}{H(\omega_n)} \\ &= \left.\frac{\Psi_n(\omega)}{H_n(\omega)}\right|_{\omega=\omega_n} \\ &= \frac{-i\omega_n}{2}\left(\frac{\sum_{m=1}^{M}\bar{A}_{nm}/c_{nm}}{\sum_{m=1}^{M}\bar{A}_{nm}}\right) \quad \text{or} \\ &= \frac{-i\omega_n}{2\bar{c}_n}, \end{aligned} \tag{18}$$

where $\bar{c}_n = \bar{c}(\omega_n)$, and $1/\bar{c}_n$ represents the weighted average of the phase velocities of all the modes of Love waves at frequency ω_n. $\bar{A}_{nm}$ is the average relative amplitude of the mth mode at frequency ω_n (equation 4). Note that the phases, being identical, cancel out in the ratio, which is thus dependent only on the frequency and the local phase velocity spectra of Love waves. $\bar{c}_n$ can be viewed as the weighted average of the phase velocities $c_{nm} = c_m(\omega_n)$ at frequency $\omega = \omega_n$ of the modes of surface Love waves plus body S waves. The ratio of amplitudes $\omega/2\bar{c}(\omega)$ will thus be running along the dashed line from $\omega/2\beta_{\max}$ at low frequencies to $\omega/2\beta_{\min}$ at high frequencies.

The Straight Line between the Limits $\omega/2\beta_{\max}$ and $\omega/2\beta_{\min}$

Perusal of Figure 8 in Lee and Trifunac (1985) shows that the ratio closely follows a straight line in the log-log plot and joins the limits $\omega/2c(\omega)$ at the low- and high-frequency ends. We also recall equations (26) and (27) in Lee and Trifunac (1985), which state that

$$\begin{aligned} \left|\frac{\Psi(\omega_n)}{H(\omega_n)}\right| &\to \frac{\omega_n}{2\beta_{\max}} \quad \text{as} \quad \omega_n \to 0, \\ \left|\frac{\Psi(\omega_n)}{H(\omega_n)}\right| &\to \frac{\omega_n}{2\beta_{\min}} \quad \text{as} \quad \omega_n \to \infty. \end{aligned} \tag{19}$$

This shows that the ratio can be approximated by the dashed line in Figure 2. Taking the lower limit at $f_0 = \omega_0/2\pi = 0.025$ Hz and the upper limit at $f_1 = \omega_1/2\pi = 50.0$ Hz, the equation of this straight dashed line in the logarithmic scale is

$$\begin{aligned} &\log\left(\frac{|\Psi(\omega)|}{|H(\omega)|}\right) \sim \log\left(\frac{\omega_0}{2\beta_{\max}}\right) + \frac{\log\left(\frac{\omega_1\beta_{\max}}{\omega_0\beta_{\min}}\right)}{\log\left(\frac{\omega_1}{\omega_0}\right)} \log\left(\frac{\omega}{\omega_0}\right) \\ &= \text{ratio}_1(\omega). \end{aligned} \tag{20}$$

In terms of periods, where $T = 2\pi/\omega$, with $T_0 = 2\pi/\omega_1 = 0.02$ sec and $T_1 = 2\pi/\omega_0 = 40.00$ sec, with $\text{FS}_\Psi(T) = \Psi(\omega)$ and $\text{FS}_H(T) = H(\omega)$, the line $\text{ratio}_1(\omega)$ becomes

$$\log\left(\frac{|\mathrm{FS}_\Psi(T)|}{|\mathrm{FS}_H(T)|}\right) \sim \log\left(\frac{\pi}{T_1\beta_{\max}}\right) + \frac{\log(\frac{T_1\beta_{\max}}{T_0\beta_{\min}})}{\log(\frac{T_1}{T_0})}\log\left(\frac{T_1}{T}\right) = \mathrm{ratio}_1(T). \quad (21)$$

Equation (21) can be viewed as an approximate empirical scaling equation for Fourier spectra of torsional motions in terms of the Fourier spectra of translational horizontal motion. The $\log(|\mathrm{FS}_H(T)|)$ can also be the logarithm of the Fourier spectrum of some recorded translational horizontal component of motion.

The straight-line approximation of the $\omega/2\bar{c}(\omega)$ is crude and less physical than the function defined in the previous section; however, it may serve as a first approximation. It does not require detailed knowledge of the physical properties of the layers at the site, except for the minimum and maximum shear-wave velocities, $\beta_{\min}$ and $\beta_{\max}$.

Ratio of Rocking to Vertical Fourier Spectra

We consider next the spectra of rocking, $\Phi(\omega)$, in terms of the spectra of the vertical translation, $V(\omega)$. The Fourier spectrum of vertical motion is determined by the contribution from the modes of Rayleigh surface waves and body P and S waves. Let $c_m(\omega)$ be the phase velocity of the mth mode of surface Rayleigh or of body S and P waves at frequency ω. We recall that the mth mode of surface waves at the nth frequency band $\omega_n \pm \Delta\omega_n$ gives the Fourier spectra of vertical translation and of rocking as

$$\begin{aligned} V_{nm}(\omega) &= A_{nm}(\omega) \\ &= \frac{\pi}{2}A_{nm}\exp[-i(\omega-\omega_n)t^*_{nm}]\exp(i\phi_n), \\ \Phi_{nm}(\omega) &= \frac{\pi}{2}\left(\frac{i\omega}{c_{nm}}\right)A_{nm}\exp[-i(\omega-\omega_n)t^*_{nm}]\exp(i\phi_n), \end{aligned} \quad (22)$$

and as zero otherwise. Within the frequency band $|\omega-\omega_n| \le \Delta\omega_n$, their ratio is

$$\frac{\Phi_{nm}(\omega)}{V_{nm}(\omega)} = \frac{i\omega}{c_{nm}}, \quad \text{with amplitude} \quad \left|\frac{\Phi_{nm}(\omega)}{V_{nm}(\omega)}\right| = \frac{\omega}{c_{nm}}. \quad (23)$$

Figure 3 shows a plot of this ratio, $\omega/c_m(\omega)$, for the five modes (1–5) of Rayleigh and body S and P (6 and 7) waves. It has the same form as equation (16), except for the factor of $\frac{1}{2}$. The curves for all seven modes have similar slopes, and more so at the high-frequency end, along the dashed line that joins the $\omega/\beta_{\max}$ at the low frequency with $\omega/\beta_{\min}$ at the high-frequency end. Combining all of the modes of Rayleigh waves and the body S and P waves, their Fourier amplitudes in the frequency domain (Lee and Trifunac, 1987) take on the same form in each of the n frequency bands $\omega_n \pm \Delta\omega_n$, as in the case of torsional spectra; their ratio $\Phi(\omega)/V(\omega)$ is also similar.

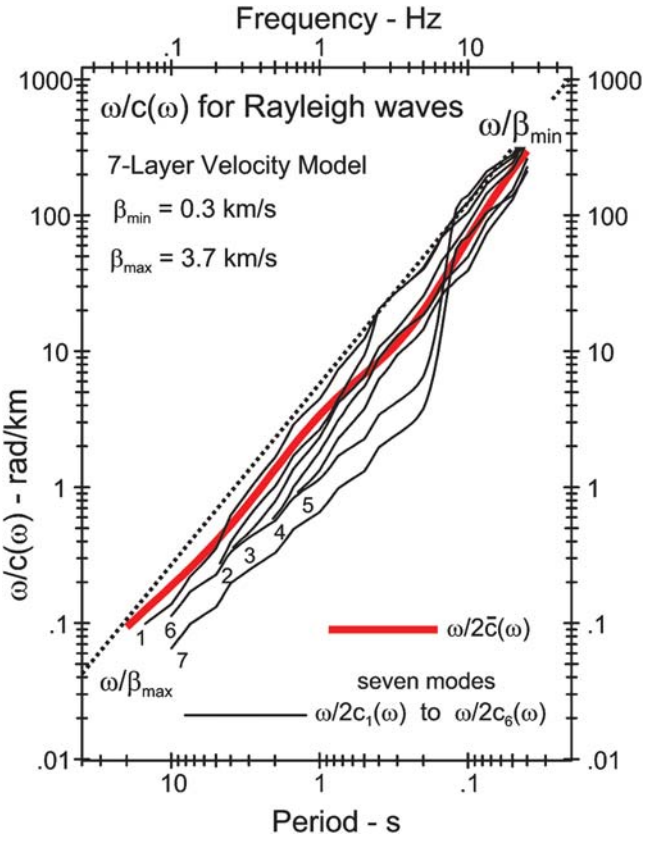

Figure 3. Ratio of frequency to phase velocities for the five modes (1–5) of Rayleigh waves, and for S and P waves (6 and 7), of a 7-layer velocity model.

In particular, at $\omega = \omega_n$:

$$\left.\frac{\Phi(\omega)}{V(\omega)}\right|_{\omega=\omega_n} = \left.\frac{\Phi_n(\omega)}{V_n(\omega)}\right|_{\omega=\omega_n} = i\omega_n\left(\frac{\sum_{m=1}^{M}\bar{A}_{nm}/c_{nm}}{\sum_{m=1}^{M}\bar{A}_{nm}}\right) = \frac{i\omega_n}{\bar{c}_n},$$

with amplitude (24)

$$\left|\frac{\Phi(\omega)}{V(\omega)}\right|_{\omega=\omega_n} = \left|\frac{\Phi(\omega_n)}{V(\omega_n)}\right| = \frac{\omega_n}{\bar{c}(\omega_n)} = \mathrm{ratio}_2(\omega)|_{\omega=\omega_n},$$

or with logarithmic scales

$$\log|\Phi(\omega_n)| = \log|V(\omega_n)| + \log[\omega_n/\bar{c}(\omega_n)],$$

where $\bar{c}_n = \bar{c}(\omega_n)$ represents the weighted average of the modes of Rayleigh and body S and P waves. The amplitudes $\omega/\bar{c}(\omega)$ run close to the straight dashed line from $\omega/\beta_{\max}$ at low frequencies to $\omega/\beta_{\min}$ at high frequencies.

The Straight Line between the Limits $\omega/\beta_{\max}$ and $\omega/\beta_{\min}$

As for torsional motions, the empirical scaling equation of rocking Fourier amplitudes, $\Phi(T)$, can be derived from

$$\left|\frac{\Phi(\omega_n)}{H(\omega_n)}\right| \to \frac{\omega_n}{\beta_{\max}} \quad \text{as} \quad \omega_n \to 0,$$
$$\left|\frac{\Phi(\omega_n)}{H(\omega_n)}\right| \to \frac{\omega_n}{\beta_{\min}} \quad \text{as} \quad \omega_n \to \infty. \tag{25}$$

The limits are the same as in the torsional case, except for the factor of $\frac{1}{2}$, which is absent here. Taking the lower limit at $\omega_0/2\pi = 0.025$ Hz and the upper limit at $\omega_1/2\pi = 50.0$ Hz, the equation of the straight line in logarithmic scale becomes

$$\log\left(\frac{|\Phi(\omega)|}{|V(\omega)|}\right) \sim \log\left(\frac{\omega_0}{\beta_{\max}}\right) + \frac{\log(\frac{\omega_1\beta_{\max}}{\omega_0\beta_{\min}})}{\log(\frac{\omega_1}{\omega_0})}\log\left(\frac{\omega}{\omega_0}\right)$$
$$= \text{ratio}_2(\omega), \tag{26}$$

or in terms of period $T = 2\pi/\omega$:

$$\log\left(\frac{|\text{FS}_\Phi(T)|}{|\text{FS}_V(T)|}\right) \sim \log\left(\frac{2\pi}{T_1\beta_{\max}}\right) + \frac{\log(\frac{T_1\beta_{\max}}{T_0\beta_{\min}})}{\log(\frac{T_1}{T_0})}\log\left(\frac{T_1}{T}\right)$$
$$= \text{ratio}_2(T) \tag{27}$$

for $T_0 = 2\pi/\omega_1 = 0.02$ sec and $T_1 = 2\pi/\omega_0 = 40.00$ sec. Equation (27) then gives an approximate empirical scaling equation for the rocking Fourier amplitude spectra in terms of the vertical translational Fourier spectra, with simple addition approximated by $\text{ratio}_2(T)$. As for torsion, this straight-line approximation of $\omega/\bar{c}(\omega)$ does not require detailed knowledge of the physical properties of layers at the site, except for the minimum and maximum shear-wave velocities, $\beta_{\min}$ and $\beta_{\max}$.

To see how well the straight lines approximate the rotation-to-translation Fourier spectral ratios, four layered velocity models have been considered. They are all the same except that the top layer is modified to have different shear-wave velocities (Table 3). Model 1 has six layers, with the top layer 0.18 km thick and with a shear-wave velocity of 0.98 km/sec. Models 2, 3, and 4 are derived from model 1 by carving the top 50 m (0.05 km) of the first layer to have shear-wave velocities equal to 0.5, 0.30, and 0.10 km/sec, leaving the remaining 0.13 km as the second layer.

Figure 4 shows the ratio of spectra of torsion to transverse horizontal translations, equation (19), for models 1 and 2, while Figure 5 shows the ratio of rocking to vertical Fourier spectral amplitudes, equation (25), for models 3 and 4. The two sets of ratios for torsion and rocking differ only by a factor of $\frac{1}{2}$. In each graph, the straight lines between $\omega/2\beta_{\max}$ and $\omega/2\beta_{\min}$ for torsion and between $\omega/\beta_{\max}$ and $\omega/\beta_{\min}$ for rocking are also plotted to illustrate how close the ratios are to the straight lines.

Empirical Scaling of Torsional and Rocking Spectra of Strong Motion

We illustrate the empirical scaling of rotational spectra of strong motion in this article in terms of what we call the third-generation scaling equations (Lee and Trifunac, 1995) for spectral amplitudes of translational accelerations.

Empirical Scaling of Torsional Spectra

The empirical ratio of torsional to horizontal transverse Fourier spectra of strong-motion acceleration, namely, $|\Psi(\omega)/H(\omega)| = \omega/2\bar{c}(\omega)$, or from equation (20) in the previous section, $\log|\Psi(\omega_n)| = \log|H(\omega_n)| + \log[\omega_n/2\bar{c}(\omega_n)]$, is first written in terms of the period of the motions. Then, with $\omega = 2\pi f = 2\pi/T$, $\text{FS}_\Psi(T) = \Psi(\omega)$ and $\text{FS}_H(T) = H(\omega)$:

$$\log|\text{FS}_\Psi(T)| = \log|\text{FS}_H(T)| + \log[\pi/T\bar{c}(2\pi/T)]. \tag{28}$$

Four different versions of the empirical scaling equations for $\text{FS}_H(T)$ are described in Lee and Trifunac (1995) for the horizontal motion ($v = 0$). Here, we will use the same notation as in that paper, where $\text{Att}(\Delta, M, T)$ is a magnitude-frequency-dependent attenuation function that depends upon the representative distance Δ from the source to the site for an earthquake with magnitude M and for period T of strong motion. s stands for geological site condition, $s = 0$ for sites on sediments, $s = 1$ for intermediate sites, and $s = 2$ for sites on basement rock; h represents the depth of sediments beneath the recording site in kilometers; v stands for the component direction, $v = 0$ for the horizontal direction,

Table 3
Properties of Top Soil Layer for Soil Models 1–4

Model Number	Top Layer Depth (km)	*P*-Wave Velocity (km/sec)	*S*-Wave Velocity (km/sec)	Density (g/cc)
1	0.18	1.70	0.98	1.28
2	0.05	1.00	0.50	1.20
	0.13	1.70	0.98	1.28
3	0.05	0.60	0.30	1.20
	0.13	1.70	0.98	1.28
4	0.05	0.21	0.10	1.20
	0.13	1.70	0.98	1.28

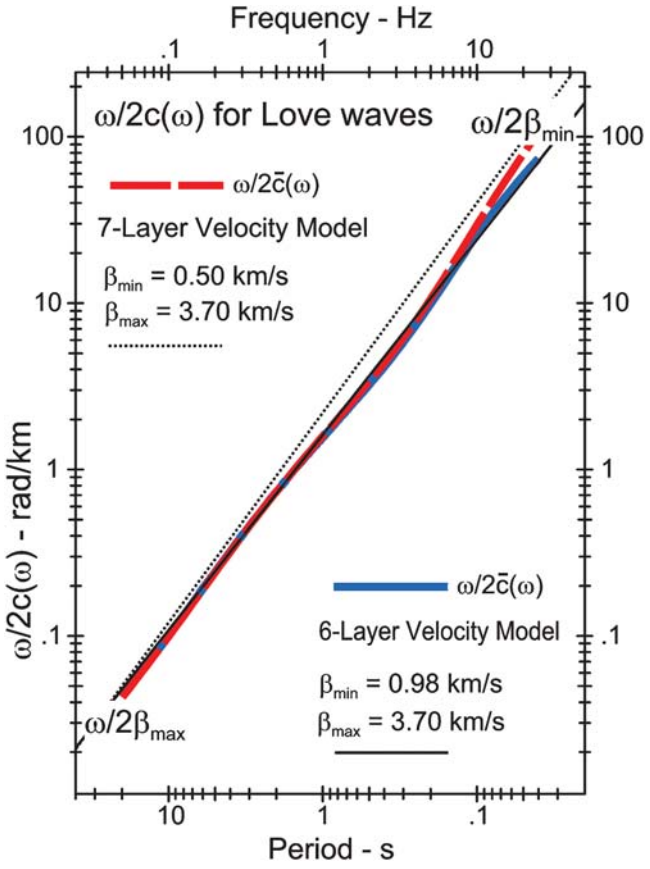

Figure 4. Ratio of Fourier spectra of torsion and of horizontal transverse translation for site models 1 and 2 in Table 3.

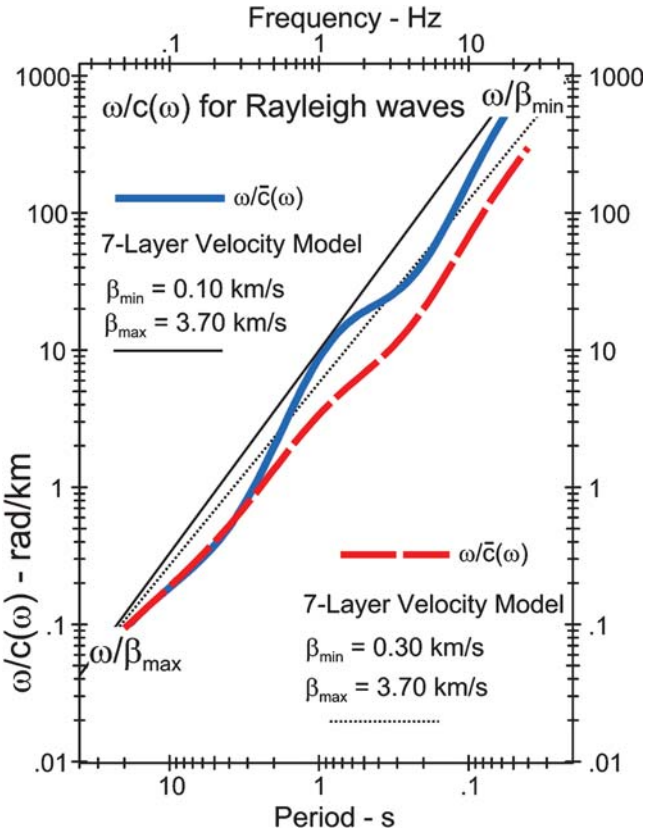

Figure 5. Ratio of Fourier spectra of rocking and of vertical translation for site models 3 and 4 in Table 3.

and $v = 1$ for the vertical motions; s_L stands for the soil type at the site, $s_L = 0$ for the rock soil site, $s_L = 1$ for the stiff soil site, and $s_L = 2$ for the deep soil site; it is represented by the indicator variables $S_L^{(i)}$ for $i = 0$, 1, and 2, $= 1$ when $s_L = i$ and 0 otherwise; r represents the ratio $(0 \le r \le 1)$ of the distance traveled through geological basement rock to the length traveled through sediments along the wave path from the earthquake source to the site; $R_<$ represents $R_< = \min(R, R_{\max})$, where R is the epicentral distance, up to $R_{\max}$ in kilometers.

Only the scaling equations for models (i) and (ii) will be used in illustrations here. Model (i) is the model in which the geological site conditions are specified in terms of $s = 0$, 1, or 2, while model (ii) uses the depth of sediments to describe the effects of local geology:

$$\begin{aligned}\text{Models (i) or (ii): Mag} - \text{ site or depth } + \text{ soil} \\ + \text{ \% rock path multistep model } (v = 0),\end{aligned}$$

$$\begin{aligned}\log \mathrm{FS}_\Psi(T) = {} & M + \mathrm{Att}(\Delta, M, T) + b_1(T)M \\ & + b_2(T)''s \text{ or } h'' + b_4(T) + b_5(T)M^2 \\ & + \sum_{\mathrm{i}} b_6^{(i)}(T)S_L^{(i)} + [b_{70}(T)r + b_{71}(T) \\ & \times (1 - r)]R_< + \log[\pi/T\bar{c}(2\pi/T)]. \qquad (29)\end{aligned}$$

In the aforesaid models, the term $b_3(T)v$ is absent because of the prediction of torsional spectra $v = 0$. A detailed description of all of the models, (i)–(iv), for Fourier spectral amplitudes of horizontal and vertical translations, can be found in the report by Lee and Trifunac (1995).

In the following examples of the estimated spectra of rotational strong motion, the site is assumed to have the minimum and maximum shear-wave velocities, $\beta_{\min}$ and $\beta_{\max}$, equal to 0.30 km/sec and 3.70 km/sec, respectively, unless otherwise stated. Figure 6 illustrates four plots of estimated Fourier amplitude spectra, $\mathrm{FS}_\Psi(T)$, of torsion, using equation (29) and model (ii). The top two plots show examples of $\mathrm{FS}_\Psi(T)$, the spectral amplitudes for torsion, and are computed from the horizontal transverse components of acceleration-time histories from earthquakes with M 3.5, 4.5, 5.5, 6.5, and 7.5, with focal depth $H = 5$ km, at the epicenter $(R = 0$ km).

The left top plot is for the sites with stiff soil conditions $(s_L = 1)$ and with geological site conditions corresponding to basement rocks (solid lines, $h = 0$ km) and sediments (dashed line, $h = 2$ km). The estimated torsional spectra are practically indistinguishable between sites on sediments $(h = 2$ km) and basement rocks $(h = 0$ km) at the low-period end $(T < 0.15$ sec). Beyond about 0.15 sec, from intermediate to long periods, the torsional spectra become larger on sediments $(h = 2$ km) than on bedrock

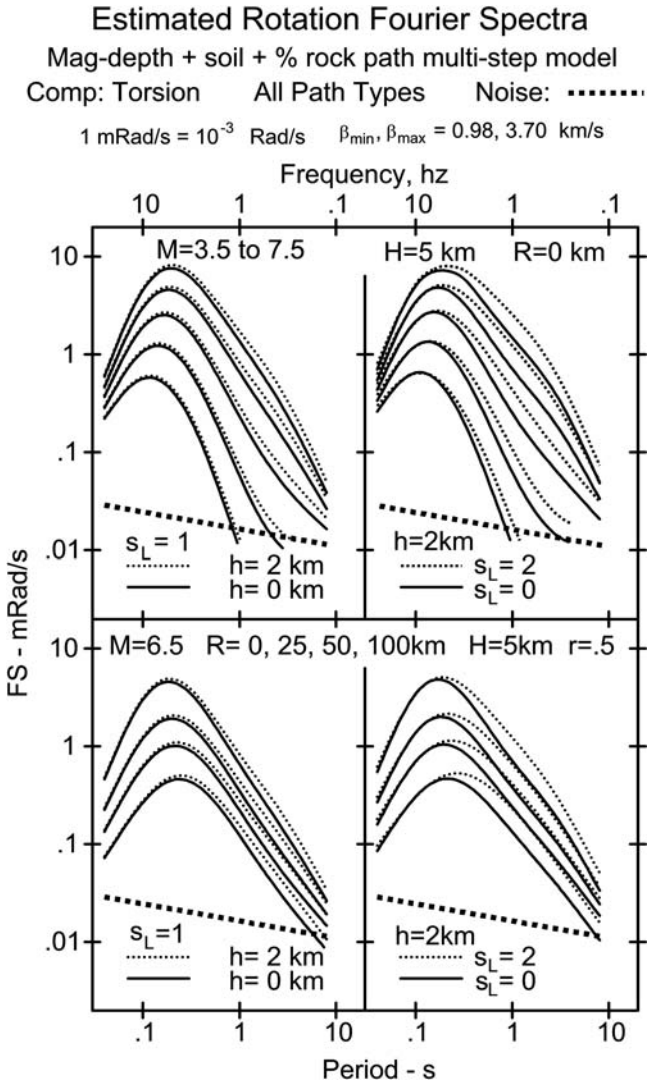

Figure 6. Estimated Fourier spectra of torsion for the Mag − depth + soil + % rock path empirical scaling model.

($h = 0$ km). This is the same as the trends observed for the most previous analyses of translational Fourier spectra (Lee and Trifunac, 1995). The top right plot is for sites on sediments ($h = 2$ km) and with rock and deep soil site conditions (solid and dashed lines for $s_L = 0$ and 2). It can be seen that the estimated torsional spectra are larger on deep soil ($s_L = 2$) sites than on rock soil sites ($s_L = 0$) in the period range from 0.04 to 8.0 sec, with the differences being small at short periods (high frequencies). This is again the consequence of the trends observed in our previous analyses of translational spectra. The bottom left and right plots are the estimated $\mathrm{FS}_\Psi(T)$ of torsion for sites with the same geological and soil types as the corresponding left and right plots on top. Here, the graphs illustrate the effect of epicentral distance R on the changes in torsional spectral amplitudes from earthquakes with M 6.5 and at focal depth $H = 5$ km. The four sets of curves with decreasing amplitudes correspond to epicentral distances of $R = 0$, 25, 50, and 100 km. The diagonal dashed lines with negative slope at the bottom of each of the spectral plots are the estimates of the $\mathrm{FS}_\Psi(T)$ amplitudes of recording and processing noise, which are obtained from the corresponding $\mathrm{FS}_H(T)$ spectral amplitudes of digitization and processing noise by addition of the term $\log[\omega/2\bar{c}(\omega)]$ as in equation (29). As for the translational case, the amplitudes of all $\mathrm{FS}_\Psi(T)$ are only valid for those periods in which the signal-to-noise ratio is not less than one.

Empirical Scaling Equations for Rocking

The empirical ratio of rocking to vertical translational Fourier spectra, $|\Phi(\omega)/V(\omega)| = \omega/\bar{c}(\omega)$, or $\log|\Phi(\omega_n)| = \log|V(\omega_n)| + \log[\omega_n/\bar{c}(\omega_n)]$, can be written in terms of the period with $\omega = 2\pi f = 2\pi/T$. Then, denoting $\mathrm{FS}_\Phi(T) = \Phi(\omega)$ and $\mathrm{FS}_V(T) = V(\omega)$ gives

$$\log|\mathrm{FS}_\Phi(T)| = \log|\mathrm{FS}_V(T)| + \log[2\pi/T\bar{c}(2\pi/T)]. \quad (30)$$

In the scaling equations of $\mathrm{FS}_V(T)$ for the vertical motion, $v = 1$, so that the term $b_3(T)v$ becomes just $b_3(T)$. With all other scaling variables defined as before:

$$\begin{aligned}\text{Models (i) or (ii): Mag} - \text{ site or depth } + \text{ soil}\\ + \text{ \% rock path multistep model (for } v = 1),\\ \log \mathrm{FS}_\phi(T) = M + \mathrm{Att}(\Delta, M, T) + b_1(T)M\\ + b_2(T)''s \text{ or } h'' + b_3(T) + b_4(T)\\ + b_5(T)M^2 + \sum_i b_6^{(i)}(T)S_L^{(i)} + [b_{70}(T)r\\ + b_{71}(T)(1-r)]R_< + \log[2\pi/T\bar{c}(2\pi/T)].\end{aligned} \quad (31)$$

Figure 7 illustrates four plots of estimated Fourier amplitude spectra, $\mathrm{FS}_\Phi(T)$, of rocking, this time using equation (31) for model (i). The top two plots show examples of $\mathrm{FS}_\Phi(T)$ for rocking computed from the vertical components of acceleration-time histories from earthquakes with M 3.5–7.5, for focal depth $H = 5$ km, and at the fault ($R = 0$ km).

The top left plot is for the sites with stiff soil conditions ($s_L = 1$) and with geological site conditions corresponding to sediments (solid lines, $s = 0$) and basement rocks (dashed line, $s = 2$). The estimated rocking spectra are slightly higher on basement rocks ($s = 2$) than on sediments ($s = 0$) at the short period end for $T < 0.15$ sec. For long periods, this trend is reversed, and the spectra become larger on sediments ($s = 0$) than on bedrock ($s = 2$). This is again the consequence of the trends observed in our previous analyses of translational Fourier spectra (Lee and Trifunac, 1995). The top right plot is for the sites on sediments ($s = 0$) and on rock soil (solid lines, $s_L = 0$) or deep soil (dashed lines, $s_L = 2$) sites. The estimated spectra are higher on deep soil ($s_L = 2$)

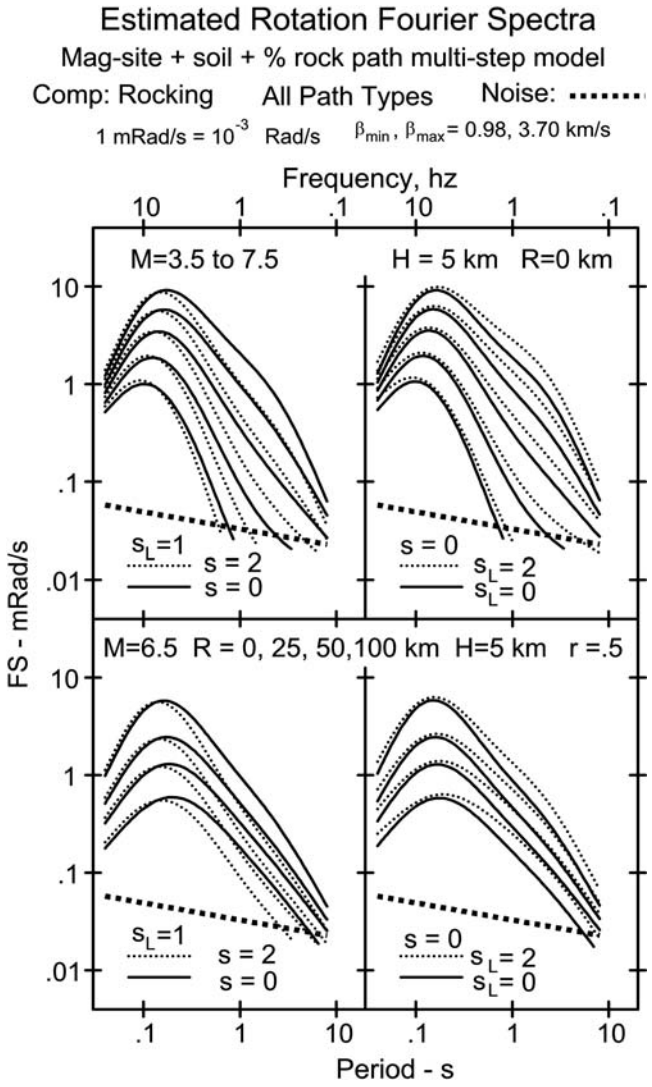

Figure 7. Estimated Fourier spectra of rocking for the Mag − site + soil + % rock path empirical scaling model.

sites than on rock soil sites ($s_L = 0$) in the entire period range from 0.04 to 8.0 sec, with the differences being minor at the short period end. The bottom left and right plots show the estimated $FS_\Phi(T)$ of rocking for sites with the same geological and soil types as the previously mentioned corresponding left and right plots. Here, the graphs illustrate the effect of epicentral distance R on the changes of rocking spectral amplitudes, from earthquakes with M 6.5 and focal depth $H = 5$ km. The four sets of curves with decreasing amplitudes correspond to epicentral distances $R = 0$, 25, 50, and 100 km. The lower right plot shows that at all distances considered, the spectral amplitudes of rocking are larger on deep soil ($s_L = 2$) sites than on rock ($s_L = 0$) soil sites at all periods, although the difference is only slight at short periods. The diagonal dashed lines with negative slope at the bottom of each of the spectral plots represent the average $FS_\Phi(T)$ spectral amplitudes of recording and processing noise.

Rotational Spectra at Pacoima Dam Site

Next, we consider the estimation of rotational spectra from the translational components of the Fourier spectra of recorded strong motion. We illustrate this for accelerograms recorded at Pacoima Dam, in California, during the 9 February 1971 San Fernando earthquake. The S74° W (horizontal) component had a peak acceleration of 1055 cm/sec^2 and a peak displacement of 10.82 cm, while the vertical component had a peak acceleration of 696 cm/sec^2 and a peak displacement of 19.3 cm. The Fourier spectra of these two components are next used to estimate the corresponding torsional and rocking components of motion. Figure 8 shows the Fourier amplitudes of the horizontal component S74° W in units of in/sec and of the corresponding torsional component in units of mrad/sec ($= 10^{-3}$ rad/sec). Figure 9 shows the Fourier amplitudes of the vertical acceleration and the corresponding rocking component. The minimum and maximum shear-wave velocities chosen for this illustration, $\beta_{\min}$ and $\beta_{\max}$, are 0.30 km/sec and 3.70 km/sec.

Figure 10 shows the torsional (left) and rocking (right) time histories obtained from the inverse Fourier transform of the corresponding rotational spectra. The peak rotations of 0.3 mrad for torsion and 0.6 mrad for rocking are obtained from the calculations. It is seen that one can use this procedure to generate approximate torsional and rocking motions for every recorded translational accelerogram for which site data on $\beta_{\min}$ and $\beta_{\max}$ are available.

Discussion and Conclusions

Our estimates of peak ground rotations are based on idealized linear representation of wave motion in the homogeneous, isotropic, and horizontally layered medium and on the assumption that the representative phase velocities at the site can be approximated by a simple straight line between minimum and maximum velocities at the site when the data on $\beta_{\min}$ and $\beta_{\max}$ are available. For large amplitudes of strong motion, surface soil, sediments, and weathered rock will undergo nonlinear deformations, which will further increase the amplitudes and the complexity of the observed ground deformations and rotations. This can be illustrated in the accelerograph site at the Pacoima Dam, California. During the 1971 San Fernando earthquake (M_L 6.6), a peak ground velocity of 115 cm/sec in the N16ºW direction was recorded by an AR-240 accelerograph that was located on a rocky spine adjacent to the southern Dam abutment. Cracking of the gneissic granite-diorite and a small rock slide were observed adjacent to the instrument housing after the earthquake (fig. 5 in Trifunac and Hudson [1971]). After the earthquake, the instrument base was permanently tilted to the northwest through an angle of about 0.5º. This accelerograph site was shaken again during the 1994 Northridge earthquake (M_L 6.4, M_w 6.7) and experienced a further permanent tilt of about 3.5° in the northeast direction (Graizer, 2006).

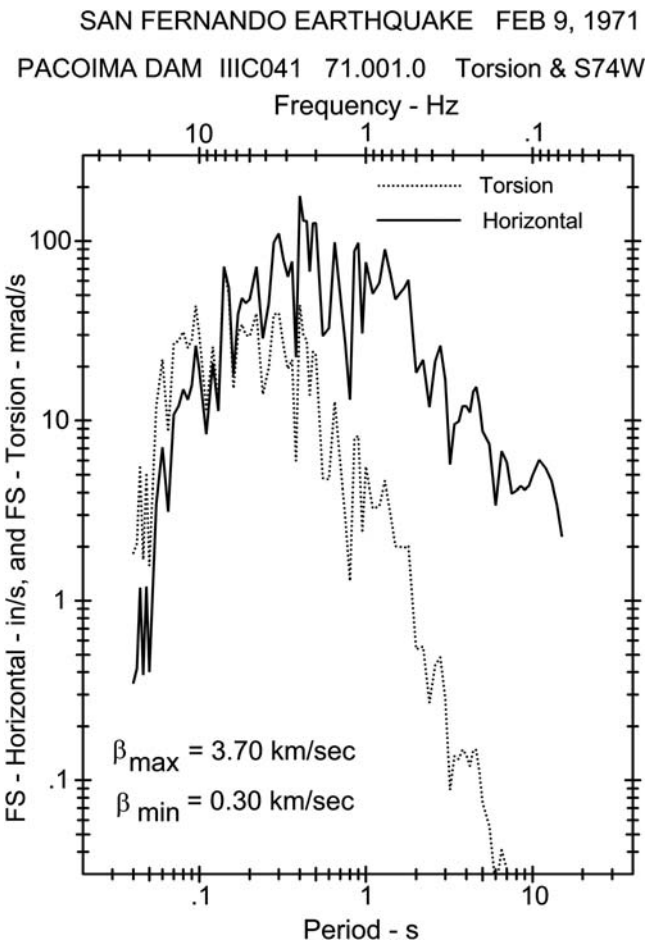

Figure 8. Fourier amplitudes of the horizontal S74°W and of the corresponding estimated torsional accelerations at Pacoima Dam during the 1971 San Fernando earthquake.

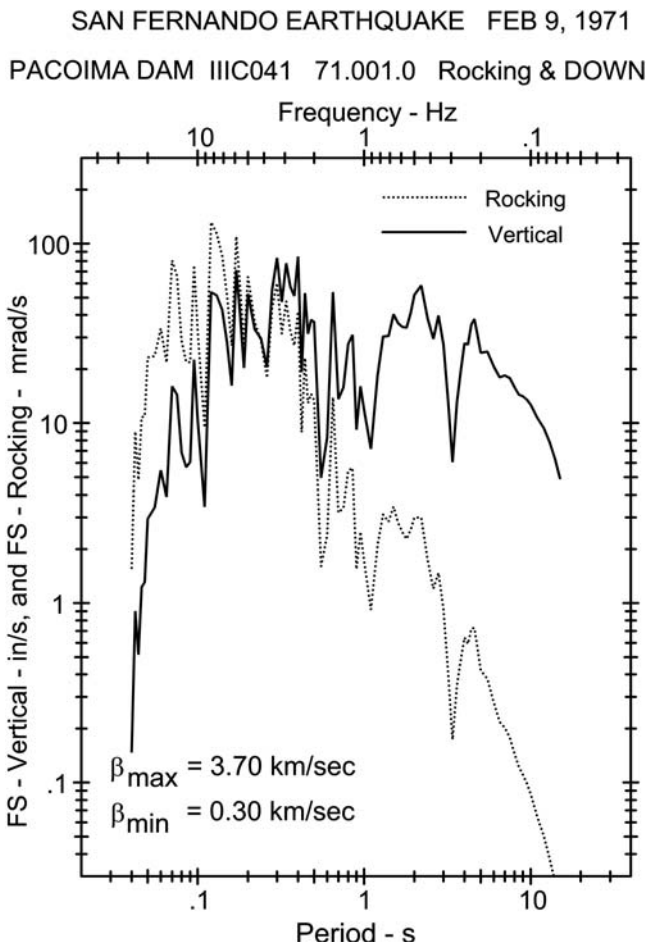

Figure 9. Fourier amplitudes of the vertical and the corresponding estimated rocking accelerations at Pacoima Dam during the 1971 San Fernando earthquake.

The permanent tilts from the aforementioned examples illustrate how large the rotations associated with the nonlinear response of near-surface deposits can be. These observations cannot be extended to predictions for other sites, as nonlinear response depends on numerous site-specific and excitation-specific factors. Nevertheless, this emphasizes the need to cautiously treat the inferences that are made only on the basis of numerical simulations and linear theory. For example, in their study of the simulations of the San Fernando earthquake, Bouchon and Aki (1982) found the maximum tilt a few kilometers from the fault to be only about 0.0007 rad and concluded that its contribution to earthquake damage is small compared to the contribution from strong-motion translations. In this article, our approximate linear analysis of the Pacoima Dam accelerogram suggests a maximum transient rocking of about 0.0006 rad. A comparison with the observed tilts at the Pacoima Dam accelerograph site suggests that the linear simulations of rotational strong-motion amplitudes, as in Bouchon and Aki's paper and this article, can underestimate the total strong-motion rotations by orders of magnitude whenever nonlinear site response can occur.

While studying large rotational velocities recorded a few kilometers away from an earthquake swarm in 1997, offshore from the Izu Peninsula in Japan, Takeo (1998, 2006) observed that those were several times larger than the rotational velocities in the numerical simulations by Bouchon and Aki (1982). However, the earthquakes that he recorded were at larger epicentral distances and had two orders of magnitude smaller seismic moments than the corresponding earthquakes in the simulation used by Bouchon and Aki (1982). Takeo (2006) proposed that "...one possible answer is that the large rotational velocities are caused by heterogeneity of slip velocity on the fault...," which is typically excluded in most numerical simulations. Takeo and Ito (1997) derived a general expression for rotational velocities of seismic waves in terms of additional torsional and curvature tensors at the earthquake source, which could explain the observations; however, this required going beyond the usual formulation of the linear theory, which is used in common forward simulations. Beyond the results of linear theory, in the near field, the nonlinear response of soil, and ultimately soil failure and liquefaction, can lead to large transient and permanent rotations, as the aforesaid example illustrates.

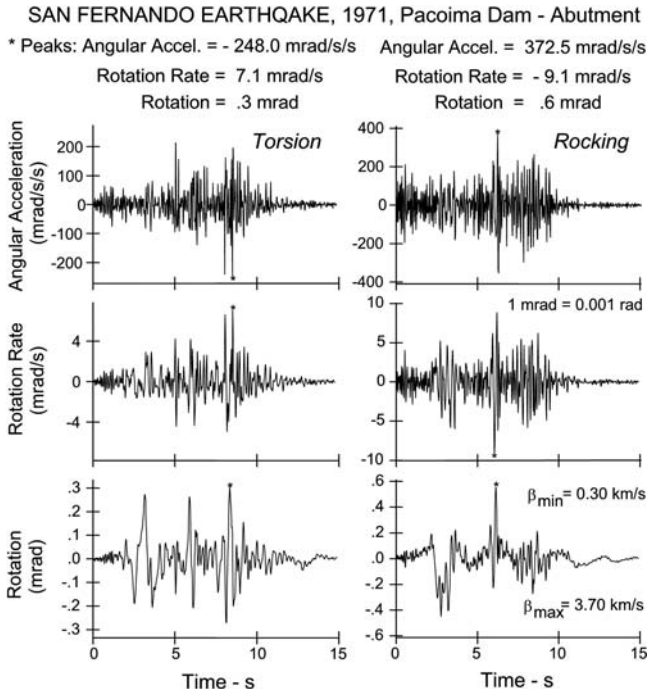

Figure 10. Torsional (left-hand panels) and rocking (right-hand panels) time histories from inverse Fourier transform of the corresponding rotational spectra.

Although we used the empirical scaling equations of translational Fourier amplitude spectra at $R = 0$ km in the previous examples, this does not mean that our spectra describe the complete motion on the fault. All of our empirical scaling equations are based on the band-pass-filtered recorded strong-motion data, typically recorded at distances from several tens of kilometers to about 100 km from the earthquake source. Consequently, the available strong-motion data, which served as a basis for the development of all existing empirical scaling equations, essentially do not contain near-field terms, which are associated with permanent fault offset and with large fault normal pulses (Trifunac, 2009b). Therefore, our results in this article only illustrate the common rotational strong-motion amplitudes beyond the distances of several tens of kilometers from the fault and do not include large rotations and large peak velocities associated with the fault slip in strong motion close to the fault.

Data and Resources

No data were used in this article. Parts of some of the plots used in this article came from published sources listed in the references.

References

Bouchon, M., and K. Aki (1982). Strain and rotation associated with strong ground motion in the vicinity of earthquake faults, *Bull. Seismol. Soc. Am.* **72,** no. 5, 1717–1738.

Graizer, V. (2006). Tilts in strong ground motion, *Bull. Seismol. Soc. Am.* **96,** no. 6, 2090–2102.

Haskell, N. A. (1953). The dispersion of surface waves on multi layered media, *Bull. Seismol. Soc. Am.* **43,** 17–34.

Hudson, D. E. (1983a). History of accelerograph development, in the *Proceedings of the Golden Anniversary Workshop on Strong Motion Seismology*, University of Southern California, Los Angeles, California, 29–56, also available at http://www.usc.edu/dept/civil_eng/Earthquake_eng/.

Hudson, D. E. (1983b). Strong motion instrumentation systems, in the *Proceedings of the Golden Anniversary Workshop on Strong Motion Seismology*, University of Southern California, Los Angeles, California, 73–86, also available at http://www.usc.edu/dept/civil_eng/Earthquake_eng/ (last accessed August 2008).

Kalkan, E., and V. Graizer (2007a). Coupled tilt and translational ground motion response spectra, *J. Struct. Eng.* **133,** no. 5, 609–619.

Kalkan, E., and V. Graizer (2007b). Multi-component ground motion response spectra for coupled horizontal, vertical, angular accelerations and tilt, *ISET, J. Earthq. Technol.* **44,** no. 1, 259–284.

Kobori, T., and I. Shinozaki (1973). Torsional vibration of structure due to obliquely incident *SH* waves, in the *Proceedings of the Fifth World Conference on Earthquake Engineering*, Vol. **1**, no. 22.

Lee, V. W. (1979). Investigation of three-dimensional soil-structure interaction, Department of Civil Engineering Report No. CE 79-11, University of Southern California, also available at http://www.usc.edu/dept/civil_eng/Earthquake_eng/ (last accessed August 2008).

Lee, V. W. (2002a). Empirical scaling of strong earthquake ground motion: part I: attenuation and scaling of response spectra, *ISET, J. Earthq. Technol.* **39,** no. 4, 219–254.

Lee, V. W. (2002b). Empirical scaling of strong earthquake ground motion: part III: synthetic strong motion, *ISET, J. Earthq. Technol.* **39,** no. 4, 273–310.

Lee, V. W. (2007). Empirical scaling of strong-motion response spectral amplitudes—a review, *ISET, J. Earthq. Technol.* **44,** no. 1, 39–69.

Lee, V. W., and M. D. Trifunac (1985). Torsional accelerograms, *Int. J. Soil Dyn. Earthq. Eng.* **4,** no. 3, 132–139.

Lee, V. W., and M. D. Trifunac (1987). Rocking strong earthquake accelerations, *Int. J. Soil Dyn. Earthq. Eng.* **6,** no. 2, 75–89.

Lee, V. W., and M. D. Trifunac (1995). Frequency dependent attenuation function and Fourier amplitude spectra of strong earthquake ground motion in California, Department of Civil Engineering Report No. CE 95-03, University of Southern California, also available at http://www.usc.edu/dept/civil_eng/Earthquake_eng/ (last accessed August 2008).

Luco, J. E. (1976). Torsional response of structures for *SH* waves: the case of hemispherical foundation, *Bull. Seismol. Soc. Am.* **66,** 109–123.

Takeo, M. (1998). Ground rotational motions recorded in near-source region of earthquakes, *Geophys. Res. Lett.* **25,** no. 6, 789–792.

Takeo, M. (2006). Ground rotational motions recorded in near-source region of earthquakes, in *Earthquake Source Asymmetry, Structural Media and Rotation Effects*, R. Teisseyre, M. Takeo, and E. Majewski (Editors), Springer, New York, Chapter 12, 157–167.

Takeo, M., and H. I. Ito (1997). What can be learned from rotational motions excited by earthquakes?, *Geophys. J. Int.* **129,** 319–329.

Thomson, W. T. (1950). Transmission of elastic waves through a stratified solid medium, *J. Appl. Phys.* **21,** 89–93.

Trifunac, M. D. (1971) A method for synthesizing realistic strong ground motion, *Bull. Seismol. Soc. Am.* **61,** no. 6, 1739–1753.

Trifunac, M. D. (1976). Preliminary empirical model for scaling Fourier amplitude spectra of strong ground acceleration in terms of earthquake magnitude, source to station distance, and recording site conditions, *Bull. Seismol. Soc. Am.* **66,** no. 4, 1343–1373.

Trifunac, M. D. (1982) A note on rotational components of earthquake motions on ground surface for incident body waves, *Soil Dyn. Earthq. Eng.* **1,** no. 1, 11–19.

Trifunac, M. D. (1989a). Dependence of Fourier spectrum amplitudes of recorded strong earthquake accelerations on magnitude, local soil con-

ditions and on depth of sediments, *Int. J. Earthq. Eng. Struct. Dyn.* **18,** no. 7, 999–1016.

Trifunac, M. D. (1989b). Empirical scaling of Fourier spectrum amplitudes of recorded strong earthquake accelerations in terms of magnitude and local soil and geologic conditions, *Earthq. Eng. Eng. Vib.* **9,** no. 2, 23–44.

Trifunac, M. D. (1990). How to model amplification of strong earthquake motions by local soil and geologic site conditions, *Int. J. Earthq. Eng. Struct. Dyn.* **19,** no. 6, 833–846.

Trifunac, M. D. (1991). Empirical scaling of Fourier spectrum amplitudes of recorded strong earthquake accelerations in terms of modified Mercalli intensity, local soil conditions and depth of sediments, *Int. J. Soil Dyn. Earthq. Eng.* **10,** no. 1, 65–72.

Trifunac, M. D. (2006). Effects of torsional and rocking excitations on the response of structures, in *Earthquake Source Asymmetry, Structural Media and Rotation Effects*, R. Teisseyre, M. Takeo, and E. Majewski (Editors), Springer, New York, Chapter 39, 569–582.

Trifunac, M. D. (2007). Recording strong earthquake motion—instruments, recording strategies and data processing, Department of Civil Engineering Report No. CE 07-03, University of Southern California, also available at http://www.usc.edu/dept/civil_eng/Earthquake_eng/ (last accessed August 2008).

Trifunac, M. D. (2008). Buildings as sources of rotational waves, in *Physics of Asymmetric Continua: Extreme and Fracture Processes*, R. Teisseyre, H. Nagahama, and E. Majewski (Editors), Springer, New York, Chapter I.5 (in press).

Trifunac, M. D. (2009a). 75th anniversary of strong motion observation—A historical review, *Soil Dyn. Earthq. Eng.* **29,** no. 4, 591–606, doi 10.1016/j.soildyn.2008.05.011.

Trifunac, M. D. (2009b). The role of strong motion rotations in the response of structures near earthquake faults, *Soil Dyn. Earthq. Eng.* **29,** no. 2, 382–393, doi 10.1016/j.soildyn.2008.04.001.

Trifunac, M. D., and D. E. Hudson (1971). Analysis of the Pacoima Dam accelerogram, San Fernando, California earthquake of 1971, *Bull. Seismol. Soc. Am.* **61,** no. 5, 1393–1411.

Wong, H. L., and M. D. Trifunac (1979). Generation of artificial strong motion accelerograms, *Int. J. Earthq. Eng. Struct. Dyn.* **7,** 509–527.

Department of Civil Engineering
University of Southern California
Los Angeles, California 90089
vlee@usc.edu
trifunac@usc.edu

Manuscript received 15 May 2008